Effect of Mesoporosity, Acidity and Crystal Size of Zeolite ZSM-5 on Catalytic Performance during the Ex-situ Catalytic Fast Pyrolysis of Biomass

Ana M. Hernández-Giménez,[a] Eleni Heracleous,[b, c] Eleni Pachatouridou,[b] Andrej Horvat,[d] Héctor Hernando,[e] David P. Serrano,[e, f] Angelos A. Lappas,[b] Pieter C. A. Bruijnincx,[a, g] and Bert M. Weckhuysen*[a]

The catalytic performance of a set of technical, zeolite ZSM-5 extruded materials have been studied in a bench scale unit for the ex-situ Catalytic Fast Pyrolysis (CFP) of lignocellulosic biomass. The set of catalysts include micro- and mesoporous materials, with and without ZrO_2-promotion, with different Si/Al ratios and with micro- and nanosized zeolite crystals. Mesoporosity, acidity and crystal size play a key role on the overall catalytic performances in terms of activity and selectivity (i.e., in their ability to obtain the highest bio-oil fraction with the lowest oxygen content), and also importantly, stability. Detailed post-mortem bulk and micro-spectroscopic studies of the solid catalysts complement the catalytic testing. The obtained results point towards coke deposits as the main cause for catalyst deactivation. Details of the nature, formation and evolution of these coke deposits revealed essential insights, which serve to evaluate the design of catalysts for the ex-situ CFP of biomass. In particular the mesoporous catalysts are overall better preserved with increasing time-on-stream and deactivate later than their microporous counterparts, which suffer from pore blockage. Likewise, it was seen that ZrO_2-promotion contributed positively in the prevention against deactivation by hard coke spreading, thanks to its enhanced Lewis acidity. The zeolite's crystal size is another important characteristic to combine the different components within catalyst bodies, ensuring the proper interaction between zeolite, promoter and binder. This is illustrated by the nanocrystalline ZrO_2/n-ZSM-5-ATP material, which shows the best catalytic performance.

1. Introduction

In an attempt to partially substitute the large amounts of fossil resources used by modern society, lignocellulosic biomass constitutes a non-edible, sustainable alternative carbon source for the production of renewable fuels, bulk and fine chemicals as well as pharmaceuticals and materials.[1–2] A common technology for liquid bio-oil production from lignocellulosic biomass is Catalytic Fast Pyrolysis (CFP).[1,3] In this process, lignocellulosic biomass is rapidly decomposed in the absence of oxygen at atmospheric pressure and high temperature, e.g. 550 °C, for short residence times. The so-called ex-situ CFP is performed in two distinct steps:[1] the first involves thermal pyrolysis of the biomass feedstock in a first reactor, after which the generated biomass vapors are upgraded over a fixed bed of solid catalyst in a second reactor. Further upgrading of the vapors or collected bio-oil is often required by, for example, subsequent (hydro)deoxygenation,[1,4] to obtain a high yield of stable bio-oil with optimal properties, i.e. the oil should be high in carbon and low in water and oxygen content to have a high heating value and be non-corrosive or viscous.[5]

[a] A. M. Hernández-Giménez, P. C. A. Bruijnincx, B. M. Weckhuysen
Inorganic Chemistry and Catalysis
Debye Institute for Nanomaterials Science
Utrecht University
Universiteitsweg 99
3584 Utrecht (The Netherlands)
E-mail: B.M.Weckhuysen@uu.nl
[b] E. Heracleous, E. Pachatouridou, A. A. Lappas
Chemical Process & Energy Resources Institute (CPERI)
Centre for Research and Technology Hellas (CERTH)
6th km Charilaou – Thermi Road, P.O. Box 361
57001 Thessaloniki (Greece)
[c] E. Heracleous
School of Science & Technology
International Hellenic University (IHU)
14th km Thessaloniki,Moudania
57001 (Greece)
[d] A. Horvat
Tovarniška cesta 10
SI-2325 Kidričevo (Slovenia)
[e] H. Hernando, D. P. Serrano
Thermochemical Processes Unit
IMDEA Energy Institute
28935, Móstoles, Madrid (Spain)
[f] D. P. Serrano
Environmental and Chemical Engineering Group
Rey Juan Carlos University
28933, Móstoles, Madrid (Spain)
[g] P. C. A. Bruijnincx
Organic Chemistry and Catalysis
Debye Institute for Nanomaterial Science
Utrecht University
Universiteitsweg 99
3584 Utrecht (The Netherlands)

Supporting information for this article is available on the WWW under https://doi.org/10.1002/cctc.202001778

As in many chemical processes, also in CFP the catalyst choice is of crucial importance to selectively attain high heating value products during long stable periods. Zeolite ZSM-5 is commonly used as catalyst for CFP of biomass, either as is[1,6] or in combination with promoters, such as Ni or Ga,[7–8] given its propensity to produce a high-quality, highly deoxygenated bio-oil. The good performance of zeolite ZSM-5-based catalysts is typically associated with their particular pore system and acidity, which enhance the different reactions involved in pyrolysis, i.e. cracking, deoxygenation, oligomerization, alkylation, aromatization.[1,6,9] However, a common limitation of zeolite ZSM-5 in this process is its poor stability. Indeed, the micropores of zeolite ZSM-5 get easily blocked by coke formation during the pyrolysis reaction.[6] The use of hierarchical ZSM-5 zeolites, which are highly mesoporous, for example as a result of desilication,[10] can improve catalyst stability with time-on-stream[11] in biomass conversion processes.[12] Hertzog *et al.* also reported on parent microporous ZSM-5 catalysts deactivating quicker than hierarchical ones on lignocellulose biomass CFM applications. Besides the improved stability, the mesoporous materials gave higher quality biofuels, producing heavier compounds with higher aromaticity and lower oxygen content.[13]

Catalyst up-scaling from lab to bench and pilot plant scale applications generally requires shaping the powdered catalytic materials into catalyst bodies to ensure mechanical strength needed to work upon continuous operation modes.[14–15] For zeolitic materials, which have poor self-binding properties, the inclusion of binders - typically, alumina, silica or clays[16–17] - is needed to attain durable catalyst bodies with the required strength and attrition resistance.[18] Yet, the selection of the specific binder or other additives, as well as the proportions used are of crucial importance, as they induce important modifications in the overall properties of the catalyst material and thus in activity.[15,19–20] Some examples of technical zeolite ZSM-5 based catalysts extruded with clay minerals as binders can be found in the literature. For instance, Pérez-Uriarte *et al.* studied the transformation of dimethyl ether (DME) into light olefins catalyzed by zeolite ZSM-5 based catalyst extrudates, showing that agglomeration with boehmite was preferred in terms of activity and stability over extrusion with bentonite.[21] Michels *et al.* reported on zeolite ZSM-5 extruded with attapulgite as clay mineral for the Methanol-to-Hydrocarbons (MTH) reaction.[22] It was found that attapulgite addition led to an attenuation of the intrinsic activity of the catalyst, while positively affecting overall catalyst stability and light-olefin selectivity. Wang *et al.* also found that attapulgite aided zeolite ZSM-5 shaped catalyst materials to enhance p-xylene selectivity and stability in toluene methylation, due to the modified acidity and enhanced diffusivity.[23]

The intrinsic catalyst' properties are fundamental characteristics to keep in mind when choosing/tailoring the right material. Nishu *et al.* recently reviewed how the pore size, shape selectivity and acidity can heavily influence the ZSM-5 catalytic properties on biomass pyrolysis.[24] Here, we compare the performance and stability of a series of technical ZSM-5/attapulgite catalyst materials in the ex-situ CFP of biomass with increasing time-on-stream, serving as guidance. The series of catalyst materials allowed several parameters to be studied: 1) the effect of auxiliary mesoporosity via desilication, which is expected to retard deactivation by limiting pore occlusion[12,25] but, at the expense of strong acidity-;[10] 2) promotion with ZrO_2, anticipated to decrease the amount of strong acid sites and provide bifunctionality, limiting excess cracking to enhance bio-oil yield;[26] and 3) the interdependence of Si/Al ratio and crystal size, with lower Si/Al ratios typically leading to increased catalyst deactivation rates,[27] while acidity depends not only on the Si/Al ratio, but also on the crystal size.[28] Therefore, the studied catalyst materials include a micron-sized, standard zeolite ZSM-5 (with a Si/Al ratio of ~18); a desilicated version of the former (Si/Al ratio of ~9), denoted as ds-ZSM-5, promoted or not with 10 wt% ZrO_2; and a nanocrystalline ZSM-5 (Si/Al ratio of ~42, n-ZSM-5), also ZrO_2-promoted.[29] All four samples were extruded with 30 wt% attapulgite as binder.

Catalytic activity studies are conducted in a continuous biomass pyrolysis bench scale unit, consisting of a fluidized bed reactor for the first stage thermal pyrolysis of oak biomass directly coupled with a second reactor for catalytic vapor upgrading (see picture in Figure S1). Technical catalysts are ground to avoid any preferential diffusion pathways within the catalytic bed in the plug-flow reactor, allowing the study to focus on the zeolite-binder interactions, isolating these from any interference that the use of the catalysts in shaped form would bring.

Catalyst materials recovered after different time-on-stream are subjected to post-mortem examination to determine the nature and location of coke formed during reaction, the main expected cause of deactivation for pyrolysis processes.[30] Coke deposits are analyzed by thermochemical analysis, namely Temperature Programmed Oxidation (TPO), and by micro-spectroscopy, namely Confocal Fluorescence Microscopy (CFM) aided by Diffuse Reflectance UV-Vis and Fourier Transform-infrared (FT-IR) spectroscopies. The effect of coke on the textural, acid and structural properties are also object of this study.

2. Results and Discussion

2.1. Fresh Catalysts Characterization

The textural properties of the catalytic materials under study (listed in Table 1) were determined by Ar physisorption and shown in Figure 1, with the isotherms and pore-size distributions of the fresh samples shown in Figures S2–S3.

The ZSM-5-ATP catalyst showed the type I isotherm accompanied by a flat H4 hysteresis loop (Figure S2a), typical for microporous materials[31] (see the high ratio S_{micro}/S_{meso} value in Fig. 1a). In the case of the desilicated ds-ZSM-5-ATP catalyst, a microporous material with additional mesoporosity, the Ar isotherm is between type I to type IIb[31] with a steep H3 hysteresis loop (Figure S2b).[32] Figure 1 illustrates that the desilicated catalyst (b) indeed presented enhanced textural properties compared to the microporous catalyst (a), as

Table 1. List of the catalyst materials under study, including an overview of the basic characteristics (see Experimental Section for complementary details).

Catalyst	Composition	Characteristics
ZSM-5-ATP	70 wt% ZSM-5/ 30 wt% attapulgite	Si/Al ~18 Crystal Size: 1–4 μm Particle size distribution d_{50}: 10 μm
ds-ZSM-5-ATP	70 wt% ds-ZSM-5 (desilicated)/ 30 wt% attapulgite	Si/Al ~9 Crystal Size: 1–4 μm d_{50}: 10 μm
ZrO_2/ds-ZSM-5-ATP	7 wt% ZrO_2/ 63 wt% ds-ZSM-5/ 30 wt% attapulgite	Si/Al ~11 Crystal Size: 1–4 μm d_{50}: 10 μm
ZrO_2/n-ZSM-5-ATP	7 wt% ZrO_2/ 63 wt% n-ZSM-5/ 30 wt% attapulgite	Si/Al ~42 Crystal Size: 30–100 nm d_{50}: 40 μm

expected.[10–11] The Ar isotherm for the ZrO_2/ds-ZSM-5-ATP material (Figure S2c) was very similar to the one obtained for ds-ZSM-5-ATP, with slightly lower microporosity (likely due to ZrO_2 deposition into the micropores), but increased mesoporosity,. The nanocrystalline material, ZrO_2/n-ZSM-5-ATP, showed a type I to IIb isotherm with a H4 hysteresis loop (Figure S2d), i.e. with a plateau at high P/Po, as often shown by nanoporous materials. At intermediate relative pressures show a steep Ar uptake, revealing the presence of textural mesoporosity. As expected,[33] the S_{BET}, S_{meso} area and V_{meso} values were substantially higher for the nanocrystalline catalyst than for the microcrystalline (without subjection to desilication) (Figure 1d cf. Fig. 1a). The pore-size distribution (Figure S3d) also showed meso- and even macropores, possibly from intergrowths created upon extrusion of the nanozeolite with attapulgite.

Bulk acidity was probed by NH_3-TPD (Figures S4 and S5) and Pyridine-FT-IR (Figure 2), to determine the concentration and the type of acidity (i.e. Brønsted/Lewis) and strength of the acid sites, respectively. The data were normalized to the total catalyst weight, given that every individual component, i.e., zeolite, attapulgite and, to a lesser extent, ZrO_2, possesses acidity. It must be mentioned that although the effect of the binder is out of focus in this work, it affects similarly to every technical catalyst selected for the study, contributing to a general reduction in Brønsted acidity while new Lewis acidity is incorporated as a consequence of ion exchange between zeolite protons and Mg^{2+} from attapulgite. This is reflected in higher selectivity (increased bio-oil yield at the expense of hindered cracking activity), and also in better stability against coke proliferation.[29,34–35]

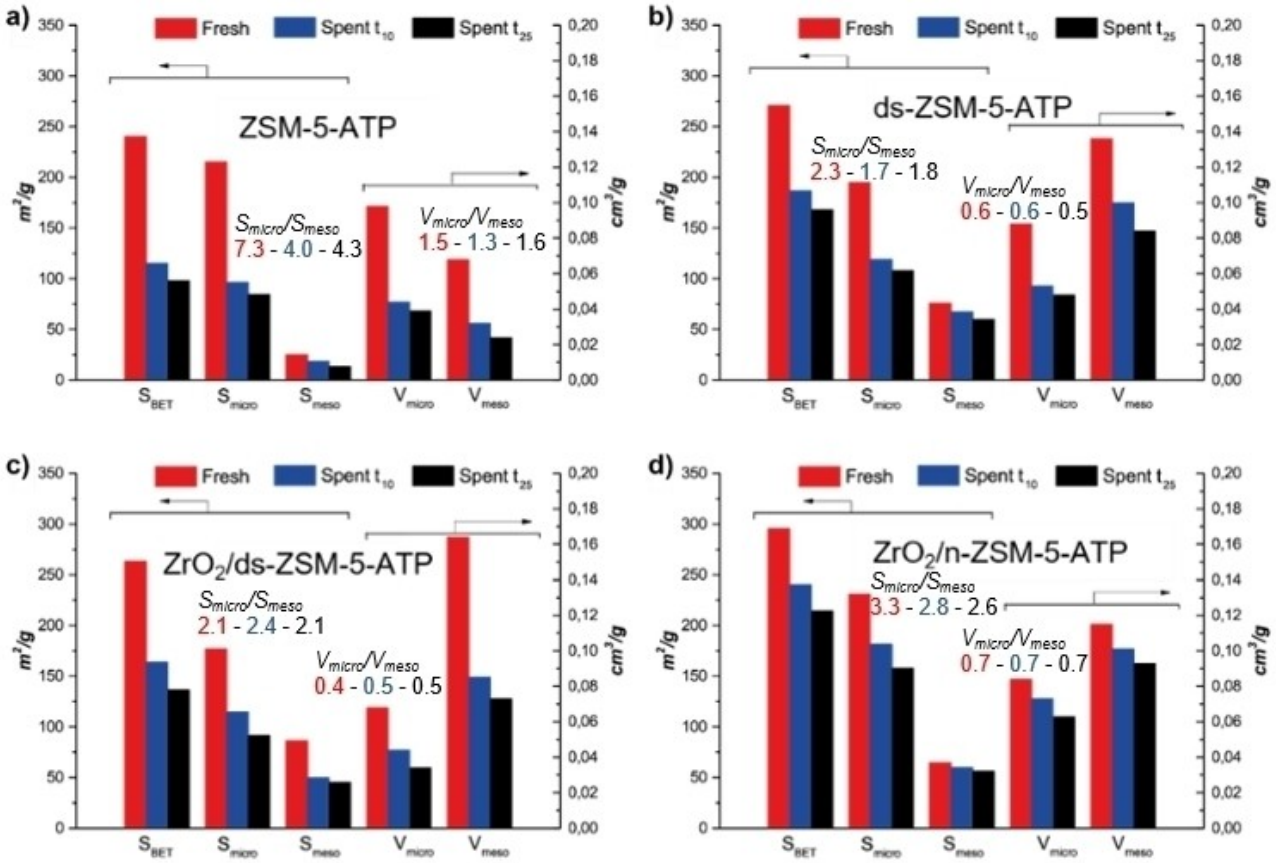

Figure 1. Textural properties for fresh (**red**) and spent catalyst materials, after the shortest -t_{10}, **blue**- and the longest -t_{25}, **black** – reaction times for catalysts: a) ZSM-5-ATP, b) ds-ZSM-5-ATP, c) ZrO_2/ds-ZSM-5-ATP and d) ZrO_2/n-ZSM-5-ATP. The evolution with time of surface and volume ratios (micro/meso) are indicated for each material, in accordance with the color code

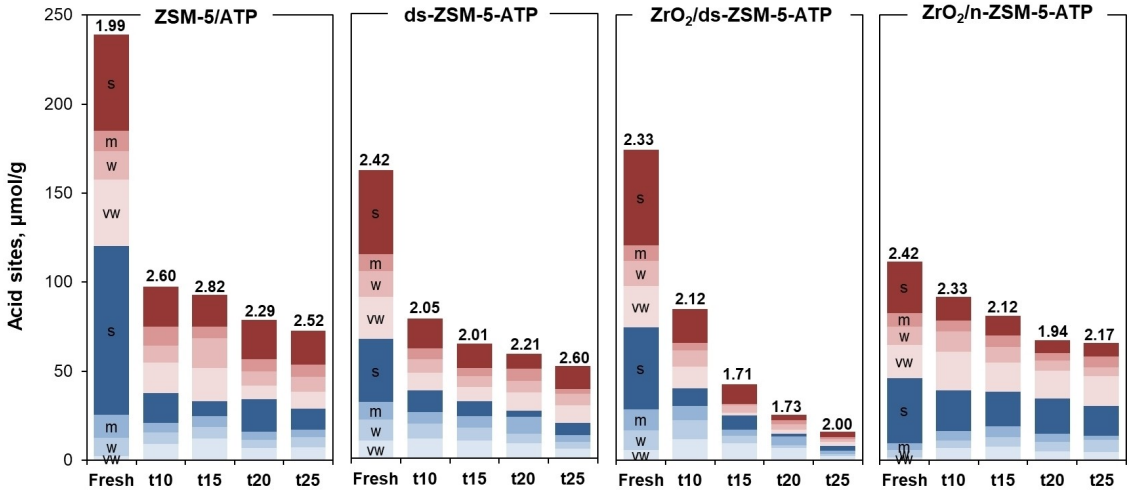

Figure 2. Acidic properties of fresh and spent samples after 10, 15, 20 and 25 min reaction for the catalysts of study determined by Pyridine-FT-IR spectroscopy (Type of sites: Brønsted (**blue**), Lewis (**red**), Strength of sites: Strong (s), medium (m), weak (w) and very weak (vw)). The values on top of the bars refer to the Lewis-to-Brønsted acid sites ratio.

The fresh ZSM-5-ATP catalyst showed very well distinguished weak and strong acid sites, as illustrated by NH_3 desorption at 235 and 415 °C (Figures S4a-b and S5a).[36–37] Pyridine-FT-IR analysis also revealed its highly acidic character, showing a large amount of strong Brønsted acid sites, attributed to the zeolite and Lewis acid sites, mainly due to the attapulgite binder.[35] Desilication of the parent zeolite led to drastic reduction of the strong Brønsted sites and a small increase in Lewis acidity (Figure 2), probably due to the formation of extra-framework Al species, as reported in literature.[10–11] In line with the Pyridine-FT-IR observations, the NH_3-TPD curve showed a shift of maximum desorption to lower temperatures, illustrative of lower acid strength (Figure S4c).[38] The addition of ZrO_2 did not modify the catalyst acidity much, with some addition of Lewis acidity being detected (Figure 2) originating from the metal oxide promoter, in accordance with the NH_3-TPD results (Figure S4d). Expectedly, ZrO_2/n-ZSM-5-ATP presented the lowest acidity of the series (Figure 2, Figure S4a,e), consistent with its higher Si/Al ratio[38–39] of ~42.

The structural integrity of the materials was determined by XRD. The XRD patterns of the fresh catalyst materials (Figure 3, red series) correspond to the orthorhombic phase of the zeolite ZSM-5 framework (PDF 00-044-0003).[39–41] The microcrystalline ZSM-5-based catalysts (Figure 3a,b,c) show sharper diffraction peaks than the nanocrystalline n-ZSM-5-based catalyst (Figure 3d), as expected.[28] When directly comparing the patterns of standard (Figure 3a) and hierarchical (Figure 3b) catalysts a drop in crystallinity is noticed for the latter, which is easily identified by the lower intensity of the low angle peaks at 2θ 9.2° and 10.3°,[42] a direct consequence of the desilication process.[10] Upon ZrO_2 incorporation to the desilicated sample (Figure 3c) the crystallinity was slightly enhanced, probably as a result of the successive calcinations performed during the synthesis. In the case of the ZrO_2/n-ZSM-5-ATP catalyst (Figure 3d) the intensity of the XRD peaks was lower, as expected for its smaller zeolite crystals.[28] The diffraction peak seen at 31.0° (2θ) for all four, fresh samples is assigned to the hexagonal quartz phase that is the most common impurity of attapulgite.[43]

3. Catalyst Performance and Deactivation

The catalyst performance and stability of the zeolite ZSM-5 based materials in the ex-situ catalytic fast pyrolysis of oak was assessed in a continuous bench scale unit (see SI for experimental details) .The tested run times (10–25 min) are long enough to determine the catalyst lifetime, as shown in a preceding work[44] where no substantial deactivation occurred at longer TOS (from 20 min to 40 min), being the early stages essential to develop the deactivation signs.

Figure 4 displays the yield of the main reaction products as a function of time-on-stream. The yield to the liquid organic products (a), essentially an inverse measure of the cracking activity, ranged between 14–24 wt%. The desilicated ds-ZSM-5-ATP sample produced the lowest content in organics, hence being the most active catalyst in terms of cracking. By contrast, the parent ZSM-5-ATP demonstrated the lowest reactivity. Despite the large reduction in Brønsted acidity induced by desilication, the formation of mesopores seems to enhance the accessibility of the bulky bio-oil molecules to the active sites thus considerably improving the cracking activity. The micro- and nano-crystalline zeolites promoted with ZrO_2 show an intermediate activity, both performing very similarly.

A good biomass pyrolysis catalyst should be able to both maximize the organic fraction and achieve a high deoxygenation degree. Oxygen removal can occur via decarboxylation, i.e. expelling of CO_2, decarbonylation (–CO) and dehydration ($-H_2O$). In terms of liquid yield, decarboxylation and dehydration is desired over decarbonylation given the more limited loss

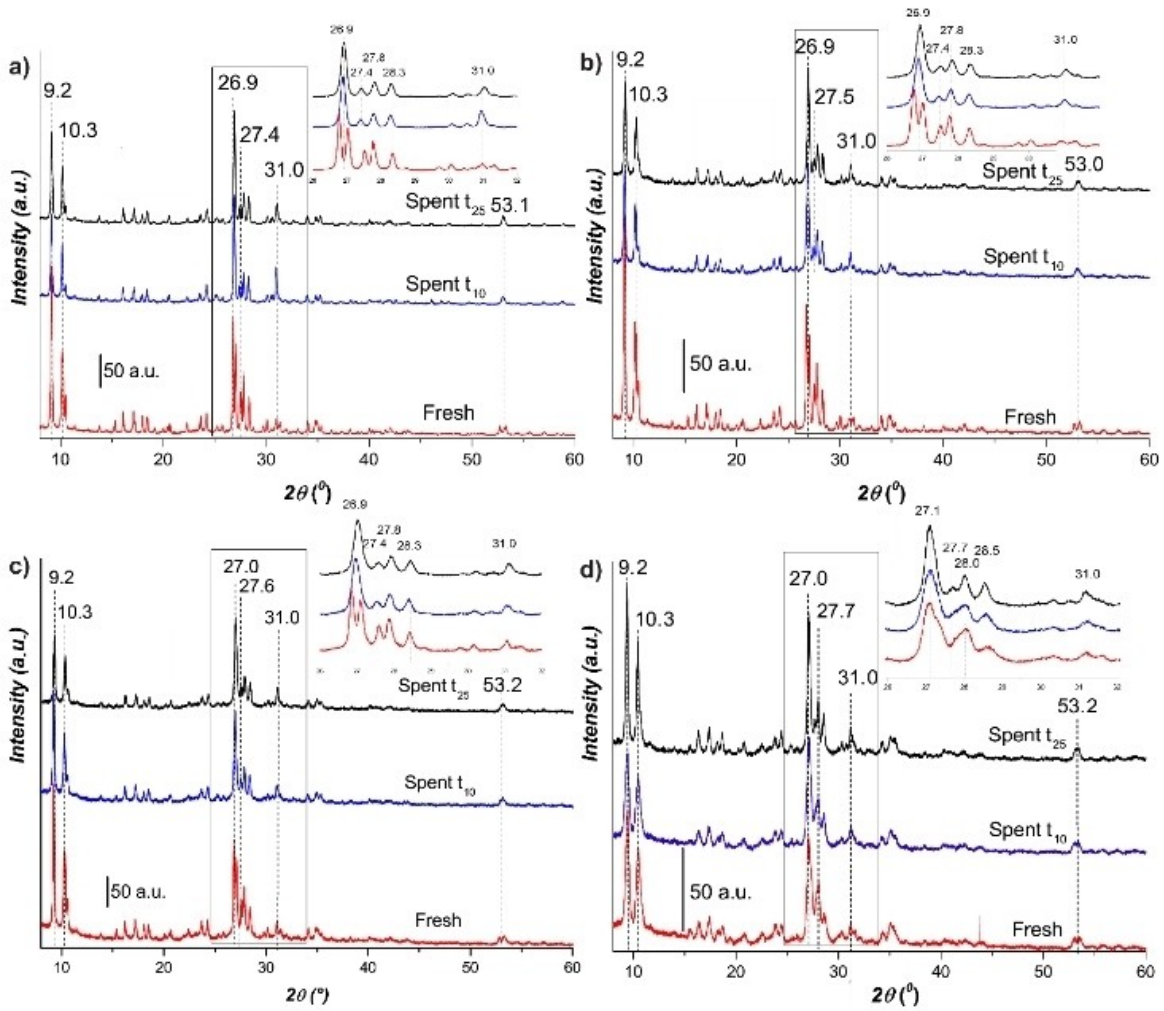

Figure 3. X-ray diffraction (XRD) patterns of fresh (**red**) and spent samples after 10 min reaction (**blue**) and after 25 min reaction (**black**) in the range $2\theta = 8$-60° for the catalysts of study: a) ZSM-5-ATP, (b) ds-ZSM-5-ATP, c) ZrO_2/ds-ZSM-5-ATP and d) ZrO_2/n-ZSM-5-ATP Insets: zoom-in of relevant diffraction peaks.

of carbon per oxygen removed. The yields to the other main reaction products, water (Figure 4b), CO_2 (c) and CO (d), clearly show that introduction of ZrO_2 improved the deoxygenation selectivity of the zeolites as it promoted decarboxylation over decarbonylation, also demonstrated in a previous work.[26] Yet, an homogeneous distribution of the ZrO_2 nanoparticles over the external surface of the zeolite crystals is required to fully ensure its role, something that occurs in the nano- (ZrO_2/n-ZSM-5-ATP) but not in the micro-sized (ZrO_2/ds-ZSM-5-ATP) catalyst.

Among the studied samples, the ZrO_2/n-ZSM-5-ATP catalyst produced the highest amount of CO_2 and the lowest amount of CO. This can be related to the mild acidity achieved by ZrO_2 addition in combination with the favorable meso- and macro-porosity of the material, in agreement with previous results.[26] The increase in CO_2 formation could also be related to the well-known ketonization activity of ZrO_2,[45] possibly promoting C–C coupling of the carboxylic acids in the bio-oil vapors to give ketones and CO_2. The superior activity of the ZrO_2/n-ZSM-5-ATP catalyst over the rest can be clearly seen in Figure 4e, giving the lowest oxygen content in the organic liquid fraction. This selective activity on the nanosized catalyst notably contributes to its improved stability with time, compared to the microsized counterparts.

Likewise, carbon deposits were also low (Figure 4f) for ZrO_2/n-ZSM-5-ATP, suggesting a lower tendency for deactivation. Using the slope of the deactivation plots as indication of the catalyst deactivation, the same trend was observed for all investigated catalysts as function of run time. Desilicated ds-ZSM-5-ATP seemed to deactivate faster, with the other three materials deactivating in a similar fashion. In general, as the reaction progresses the catalysts gradually become less active, producing more organic liquid product but with a higher oxygen content. After 25 min, the oxygen in the bio-oil increased by about 4–6 wt%. This is accompanied by a clear decrease in the cracking and deoxygenation activity with time-on-stream. Simultaneously, the accumulation of carbon on the catalyst surface increased, a likely cause of catalyst deactivation.[46] Carbon levels on the catalyst strongly depended on the pyrolysis run time. Rapid carbon accumulation up to

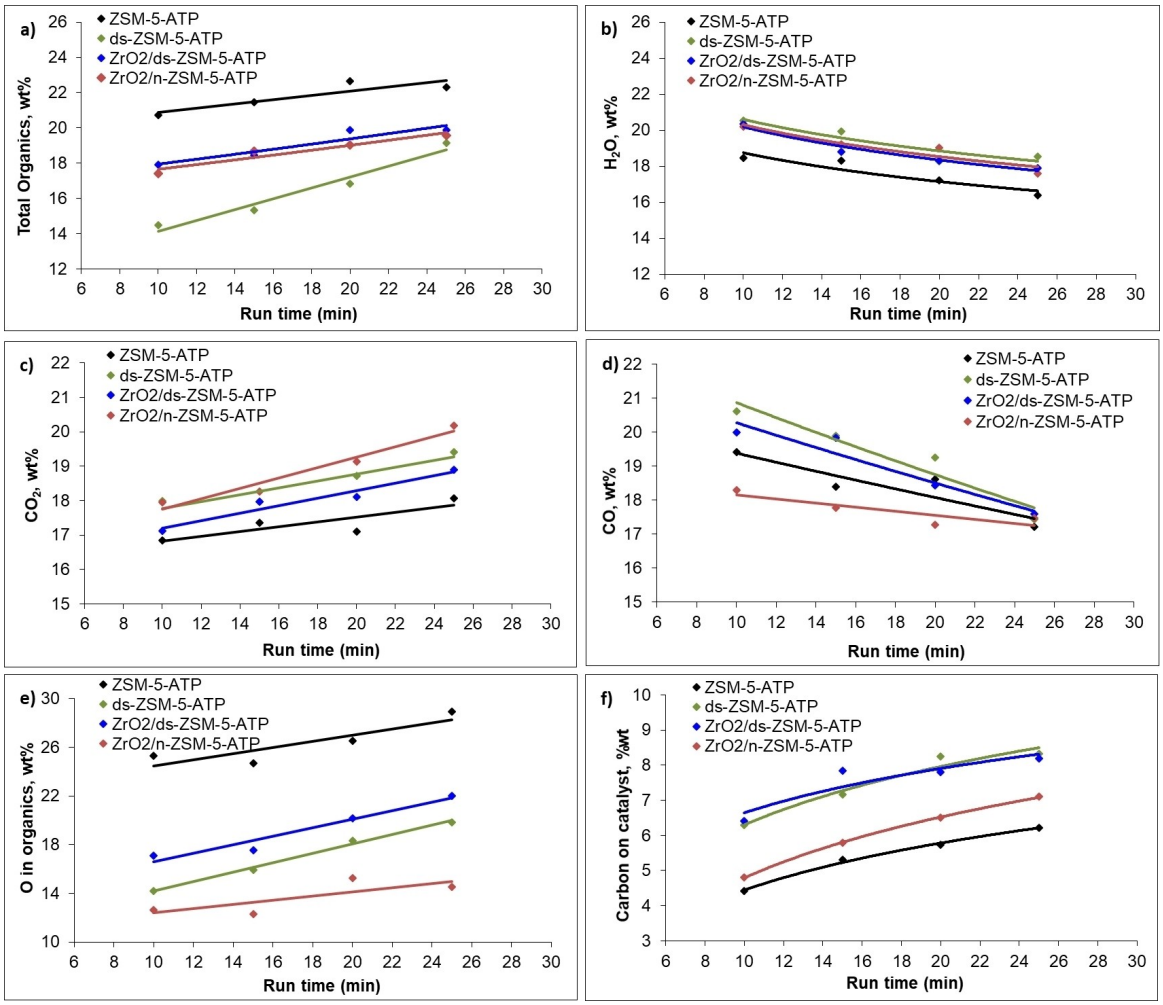

Figure 4. Yield to a) total organics (determined by difference from Karl Fischer titration and from LECO-CHN and GC-MS analyses), b) water, c) CO_2, d) CO (all three gases measured in a GC-TCD), e) amount of O in organics and f) carbon on catalyst (both measured in a LECO-800 CHN analyzer) as a function of time on stream in ex-situ fast pyrolysis of oak at bench scale for the catalysts of study.

about 5–7 wt% occurred within the first minutes of the reaction. With increasing time-on-stream, the amount of carbon depositing per time stabilized as the catalysts started to deactivate, decreasing the formation rates. It should be noted that the catalysts' deactivation is reflected in a different way in CO_2 (Figure 4c) and CO (Figure 4d) formation, with the deactivated samples producing gradually more CO_2 and less CO, coming also from the combustion of increased char (over liquid oil) in the thermal unit. This suggests that deactivation affects the active sites that favor the decarbonylation and decarboxylation reactions in a different way, in agreement with results previously reported by Vitolo *et al.*[9] and Ibáñez *et al.*[47] on the deactivation of H-ZSM-5 catalysts in bio-oil upgrading.

To complement the above-mentioned findings about deactivation as a function of time (where comparison between catalysts refer to different conversion levels), Fig. 5 represents the bio-oil oxygen content in function of the bio-oil yield, an actual way of determining the efficiency of the deoxygenation process, measuring the catalyst's deactivation impact. The data in Figure 5 show that for the same bio-oil yield (i.e. same activity degree) both ZrO_2-containing catalysts demonstrate lower oxygen content than their non-promoted counterparts (with much more pronounced effect for nanocrystalline ZSM-5 as discussed above). This points at the previously mentioned

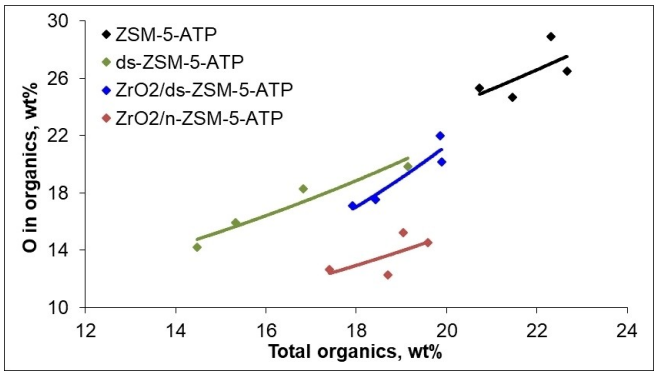

Figure 5. Bio-oil oxygen content in function of the bio-oil yield for the four catalytic materials of study.

role of ZrO_2 which improves the deoxygenation selectivity. Also based on Figure 5, it can be seen that desilicated samples (promoted and non-promoted with ZrO_2) are more affected by deactivation in terms of selectivity, as indicated by the more pronounced slope. The ZrO_2/n-ZSM-5-ATP catalyst proved again a better behavior against deactivation.

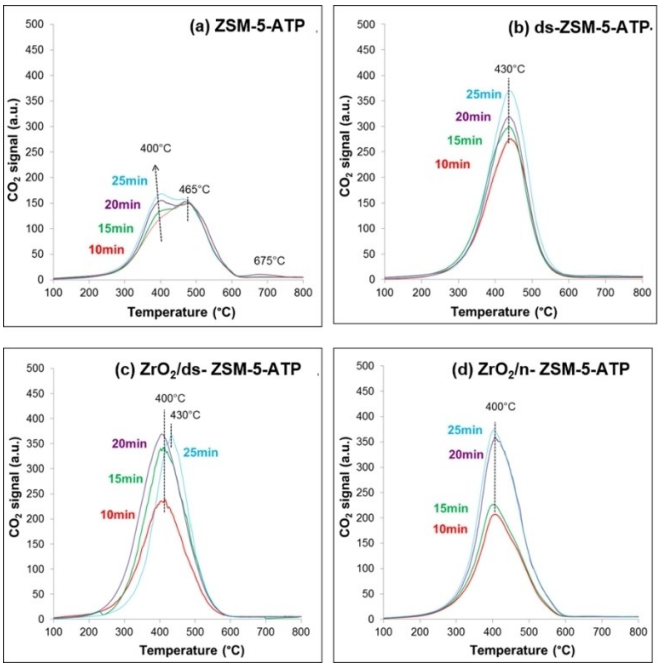

Figure 6. Temperature programmed oxidation (TPO) profiles of the catalyst materials after 10, 15, 20 and 25 min reaction for the catalysts under study: a) ZSfM-5-ATP, (b) ds-ZSM-5-ATP, c) ZrO_2/ds-ZSM-5-ATP and d) ZrO_2/n-ZSM-5-ATP.

4. Nature, Location and Effect of Coke Deposits

4.1. Nature of Coke Deposits.

The nature of coke deposited on the different catalyst materials as a function of reaction time (Figure 4f) was investigated in detail by Temperature Programmed Oxidation (TPO, Figure 6). Likewise, the nature of coke deposits was also investigated by post-mortem examination of the spent catalysts with confocal fluorescence microscopy (CFM), aided by FT-IR spectroscopy and UV-Vis diffuse reflectance spectroscopy (DRS). The main results are summed-up in Table 2, at the end of the section.

As seen in Figure 4f, coke accumulation increased with time-on-stream for all catalysts, with both desilicated materials (ds-ZSM-5-ATP and ZrO_2/ds-ZSM-5-ATP) exhibiting the highest amounts of coke in agreement with increased porosity allowing for enhanced growth. In line with this, the microporous ZSM-5-ATP catalyst showed the lowest coke weight. The ZrO_2-promoted nanocrystalline ZSM-5 exhibited, despite its high activity, a low coking tendency. The CO_2 desorption profile of the parent ZSM-5-ATP catalyst (Figure 6a) clearly suggested that different types of carbonaceous species were formed, whose nature depends on the reaction time. The main peak extended between 300–600 °C with maximum CO_2 evolution seen at 465 °C. This combustion temperature can be associated with polyaromatic coke located in the zeolite's micropores, as reported in literature.[48] The position and size of this peak did not change with time-on-stream, confirming that coke was

Table 2. Summary of the main deactivation coke signs and effects on the different catalytic materials of study.

Catalyst	ZSM-5-ATP	ds-ZSM-5-ATP	ZrO_2/ds-ZSM-5-ATP	ZrO_2/n-ZSM-5-ATP
Coke content [wt%]	4.4% (10′)→6.1% (25′)	6.3% (10′)→8.2% (25′)	6.5% (10′)→8.1%(25′)	4.9% (10′)→7.1% (25′)
Type of coke and location	poly-aromatic (e.g. pyrene) in zeolite micropores; pre-graphitic (e.g. coronene) on zeolite external surface; naphthalenes/anthracenes/poly-aromatics in rich-in-binder domains	poly-aromatic (>3 aromatic rings) alongside zeolite mesopore walls. anthracenes/poly-aromatic in rich-in-binder domains	poly-aromatic alongside zeolite mesopore walls; softer coke in ZrO_2-covered areas; anthracenes/poly-aromatic in rich-in-binder domains	poly-aromatic alongside the entire catalyst (meso-, macro-, externally) with preferential location on crystal voids/ intergrowths
Textural properties effects	microporosity occlusion; surface area severely dropped	microporosity affected within 10 min; mesoporosity well preserved	micro-and mesoporosity affected equally	micro- and mesoporosity slightly dropped
Acidity effects	strong decrease of Brønsted active sites within 10 min reaction (micropores), afterwards (25 min) Lewis sites decrease (external)	important but gradual decrease in strong acid sites (Lewis and Brønsted)	important decrease in strong acid sites (Lewis and Brønsted)	gradual decay of Brønsted and Lewis acid sites; strength well preserved
Crystallinity effects	crystallinity drop (organics and re-dispersion of attapulgite) and (irreversible) zeolite phase change from orthorhombic to tetragonal	(reversible) crystallinity distorted by coke and attapulgite re-dispersion; no phase change	(reversible) crystallinity distorted by coke and attapulgite re-dispersion; no phase change	(reversible) crystallinity distorted by coke and attapulgite re-dispersion; no phase change
Catalytic effects	deactivation by pore blockage, poor deoxygenating capacity	deactivation by active site poisoning, accentuated cracking activity (opposite to bio-oil yield), selectivity (deoxygenating capacity) diminished	deactivation by active site poisoning, gradual increase of CO_2 formation in detriment of CO, selectivity severely affected	activity and selectivity better preserved

mostly deposited in the micropores during the first minutes of the reaction. A second, well-defined peak with a maximum at the lower temperature of 400 °C, increased in intensity as function of time, corresponding to softer coke deposited on the surface and between the zeolite crystals (voids). The increase with reaction time indicates that once the micropores are blocked, low amounts of hydrogen-rich coke are gradually formed on the external surface of the zeolite ZSM-5. Both types of coke are thought to be formed by condensation–degradation of certain oxygenated bio-oil components, in particular those derived from lignin pyrolysis because of their greater ability to polymerize.[49] Finally, for the 20 and 25 min samples, a third small peak developed at 675 °C, associated with hard graphitic coke.

The shape of the CO_2 evolution curves of the desilicated ds-ZSM-5-ATP samples (with and without ZrO_2) and the ZrO_2-impregnated nanocrystalline ZSM-5 all looked similar and different from the standard ZSM-5-ATP catalyst, with one wide peak extending from 200–600 °C. For ds-ZSM-5-ATP (Figure 6b), the maximum was centered at 430 °C and shifted to lower temperature (400 °C) for the ZrO_2-promoted sample (Figure 6c). This suggests that coke was of softer nature in the desilicated samples, hence easier to oxidize, possibly located in the mesopores. The nanocrystalline material (Figure 6d) also showed the presence of soft coke, which might be located in the mesopores/macropores, on the external surface and in intracrystalline voids. Lower residence times of reactants/intermediates in the larger pores could also contribute to the softer nature of the carbonaceous deposits in these samples. ZrO_2 seemed to limit the formation of more extensive polyaromatic coke species. Similar findings have been reported for the deactivation of mesoporous zeolites MFI in the MTH reaction which upon probing of the location of coke by Ar adsorption measurements showed that in the mesoporous zeolites the coke was formed mainly on the walls of the mesopores (external coke), while in the conventional zeolites it was located mainly inside the micropores (internal coke).[50] However, it should be noted that the amount of coke formed on the desilicated and nanocrystalline ZSM-5 technical samples was higher than that on the standard ZSM-5-ATP catalyst, probably due to both the higher activity of the former and to the mesopores/macropores providing more space for the coke to grow.

4.2. Location of Coke Deposits.

Visualization of coke alongside the tailored catalysts allows to understand the evolution of its spreading, what contributes for the catalyst design optimization. Coke, given its fluorescent properties, allows for its spatial distribution within the catalyst to be determined by confocal fluorescence microscopy.[51] Neither the fresh zeolite crystals nor the binder aggregates show fluorescence in the absence of any organic compound. The CFM, UV-Vis DRS and FT-IR micro-spectroscopy data are shown in Figure 7, with Figure 8 as well as Figures S6-S8 showing some additional representative CFM images. For the sake of clarity, only images and corresponding spectral information of the shortest, t_{10} (Figure 8, Figure S6) and longest reaction time, t_{25} (Figures S7 and S8) are included.

Different regions can be distinguished in the FT-IR microscope image of the catalyst surface of ZSM-5-ATP after 10 min of reaction (Figure 7a). Most abundant are regions with high presence of black coke (highlighted in red); other less abundant regions seem practically free of coke (see evident difference in color of the region highlighted in green, Fig.7a). The corresponding FT-IR spectra of these regions (Figure 7d) showed many similarities to the FT-IR spectra of both pure ZSM-5 (black series) and attapulgite (orange), respectively, for which both intrinsic SiO_2 bands and coke and aromatic bands (1626, 1575 cm^{-1}) dominate. An FT-IR feature characteristic of zeolite ZSM-5[28] and lacking in attapulgite[52] is the band at 1210 cm^{-1}. This band was absent in the lighter zones, suggesting these to be rich-in-binder domains. Analogously, the obscure regions do show the 1210 cm^{-1} vibration and therefore may be rich-in-zeolite. The optical microscope images (Figure 7b) also showed the presence these light (in green) and obscure zones (in blue or red with increasing darkening). The UV-Vis DRS spectra of the highlighted zones (Figure 7e), show absorption over the entire visible wavelength range due to of the (black colored) poly-aromatic coke (with more than 3 aromatic rings), and even poorly H-containing graphite-like species (given the baseline contribution),[53–54] confirming the findings by TPO analysis in section 3.1. Note that rich-in-zeolite regions present zones with harder (black coke seen in region highlighted in red) and softer coke (see less dark colored region in blue). While the former might be located in the zeolites micropores, the softer of H-richer coke might be preferentially located on the zeolite external surface.[48] On the other extreme, the lighter region (highlighted in green) showed lower absorption than the regions ascribed to zeolite domains, with a peak maximum at around 400 nm (Figure 7e), where substituted benzene carbocations or naphthalene-like species absorb light.[55] Figure 7c shows the surface of the spent ZSM-5-ATP catalyst irradiated by the lasers of the CFM set-up. The optically obscure zeolite(-rich) domains, highlighted in blue and red, give areas of high fluorescence. The corresponding emission spectrum (Figure 7f) of the lighter/brighter region (blue) suggests the presence of anthracene-like and poly-aromatic types of coke, emitting light at wavelengths close to 500 and 600 nm, respectively.[56] The highlighted region in red showed more poly-aromatics than anthracenes. In contrast, the region in green (Figure 7c) suggested to be more concentrated (rich-) in binder, showed less fluorescence with a more equal distribution of naphthalenes, anthracenes and poly-aromatics, as indicated by its emission spectrum (Figure 7f).

According to Magnoux and Guisnet studies[57–58] -based on the ZSM-5 type of zeolite, the high reaction temperature (450 °C) and the high coke content (> 4.5 %)- pyrene-like species (as representative molecule of poly-aromatics, still soluble coke fraction, might be sheltering into the catalyst pores. These might be of size compatible with the ZSM-5 channel intersections, i.e. around 9 Å. Besides, coronene/pre-graphitic type of

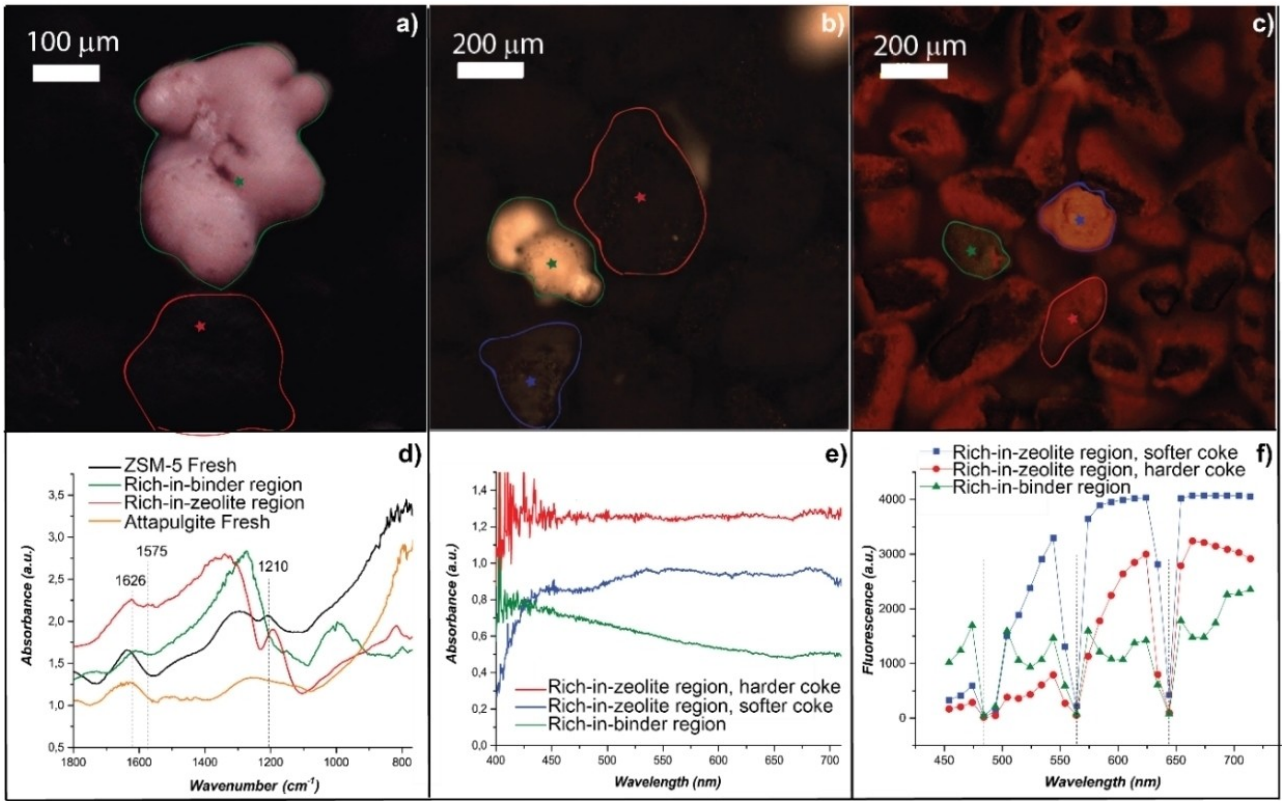

Figure 7. Visualization of spent ZSM-5-ATP catalyst after 10 min of reaction. a) Image obtained with IR microscope and d) corresponding spectral information suggest the obscure zone highlighted in red to be rich-in zeolite; in the fingerprint of the green region is more similar to attapulgite. b) Optical image obtained with the UV-Vis diffuse reflectance microscope showing obscure (red, blue) and light (green) regions and e) the corresponding absorption spectra. c) Confocal fluorescence microscopy (CFM) image showing obscure and light regions, and f) corresponding emission spectra. Dashed vertical lines represent the excitation lasers, fixed at $\lambda = 488$, 561 and 642 nm.

(non-soluble, of several nm size) coke might be surrounding the zeolite crystals fraction.

Compared to the microporous ZSM-5-ATP catalyst (Figure 8a), the CFM images of ds-ZSM-5-ATP (Figure 8b) barely showed any fluorescence because of the large amount of coke formed on the desilicated sample, which impedes light emission.[56] This is in line with the TPO results which showed more coke on the desilicated ds-ZSM-5-ATP than on the microporous ZSM-5-ATP catalyst (see values expressed in Table 2). Typically, coke growth is associated with a higher amount of strong Brønsted acid sites,[53,58] which is normally higher for lower Si/Al ratio -at a given crystal size-.[12,59] Yet, that more coke was present on ds-ZSM-5-ATP than on ZSM-5-ATP catalyst is associated with the larger pore diameters of the desilicated material, which allows coke to grow in a bulkier manner.[12,57] In these large confinements propagation of coke might also be enhanced by a bimolecular hydride transfer effect, as reported in literature.[61–63]

Fluorescence intensity was also very low for ZrO_2/ds-ZSM-5-ATP (Figure 8c) except for some minor regions looking especially intense, highlighted in blue. These scarce fluorescent regions are characterized by softer coke and thus may be associated with ZrO_2-promoted zeolite-rich domains. Indeed, ZrO_2 is known to cause an enhancement of the Lewis acid sites -thought to help on limiting the formation of deactivating poly-aromatic coke,[64] in line with the TPO results that showed a decrease in the maximum temperature of coke combustion in the ZrO_2-promoted samples. This segregated binder- (green) and zeolite-domains (better observed in Figure 8f) indicate that the ternary ZrO_2-impregnated ds-ZSM-5 catalyst is not a very homogeneous mixture. For the nano-sized ZrO_2/n-ZSM-5-ATP regions (Figure 8d) neither rich-in-zeolite or rich-in-binder regions can be distinguished. This suggests better mixing of the clay with the nanocrystals, resulting in a more homogeneous material than the micrometer-sized zeolite sample.

CFM images at higher magnification of zeolite(-rich) regions of the four catalysts (Figure 8e-h, complemented with binder (-rich) domains in Figure S6) show highly fluorescent spots (red series) at the single particle level, presumably corresponding to the individual zeolite crystals. Such highly fluorescent zeolite crystals can also be found in the images of rich-in-binder regions (Figure S6), but are less abundant. The emission spectra are more intense at the individual spots, i.e. zeolite crystals, but the same profile as recorded for the entire zeolite-rich domains, as expected. Emission spectra suggest a large concentration of naphthalenes/anthracenes (emitting light between 400–500 nm) and poly-aromatics (above 550 nm). For the ZrO_2/n-ZSM-5-ATP catalyst the differences between the so-called

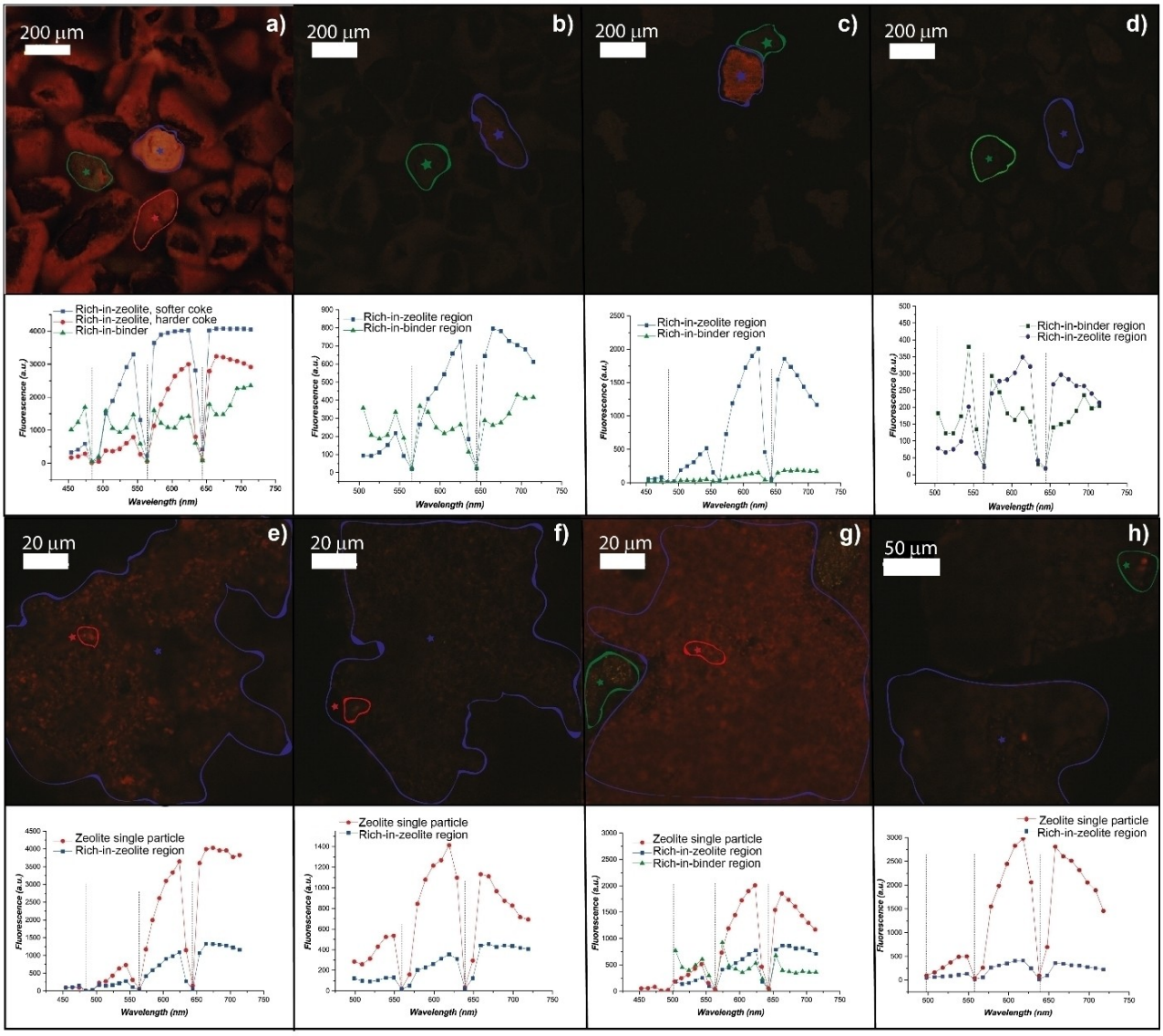

Figure 8. Confocal fluorescence microscopy (CFM) images, under 10 (a–d) and 100 times magnification (e-h), and corresponding spectra (below) of colored zones of ZSM-5-ATP (a,e), ds-ZSM-5-ATP (b,f), ZrO_2/ds-ZSM-5-ATP (c,g) and ZrO_2/n-ZSM-5-ATP catalysts (d,h) after 10 min of catalytic pyrolysis. Dashed vertical lines represent the excitation lasers, fixed at $\lambda = 488$, 561, 642 nm.

obscure/zeolite-rich (blue) and light/binder-rich (green) domains (h) were less distinct than for the microcrystalline samples (and in particular the ZrO_2/ds-ZSM-5-ATP, in Figure 8g), what might indicate again that the nanocrystalline sample is better mixed with the attapulgite binder.

With increasing reaction time, the fluorescence significantly dropped, as evidenced by the CFM images taken after 25 min of reaction (Figures S7 and S8). This is indicative of the progressive increase in coke size and amount and its transformation into more poly-aromatic/graphitic type species that eventually preclude light emission. Such larger and more condensed coke fragments are in line with TPO analyses, which showed increased CO_2 released upon combustion and higher combustion temperatures. These changes appeared to be more gradual for the nanocrystalline compared to the microcrystalline catalysts, as the differences in spent samples after 10 (Figure 8h) and after 25 min reaction (Figure S8d) were less obvious. This might indicate that coke remained of similar nature on the ZrO_2/n-ZSM-5-ATP catalyst at different time-on-stream, in line with the TPO measurements where no change in the maximum temperature of coke oxidation was recorded for the deactivated samples.

4.3. Effect of Coke Deposits.

Coke buildup is well evidenced by the general attenuation of the textural properties after reaction, worsening with longer reaction times. After 10 min reaction the fresh ZSM-5-ATP catalyst had suffered a dramatic drop in microporosity and

surface area to nearly the half of the initial (see blue series cf. red in Fig. 1a, and the disappearance of the hysteresis loop in Figure S2a). Upon application of the *t*-plot and BJH methods -for estimating micro- and mesoporosity, respectively- is seen a strong occlusion of the pores by coke formation within the first 10 min of reaction (Figure 1a). Clearly, pore blockage by coke deposition[57] is pointed as the main deactivating fpactor for the ZSM-5-ATP catalyst. A further but milder drop after 25 min reaction was seen, supporting the observations from TPO that indicated that most of the coke was formed in the first minutes of the reaction in the micropores (Figure S3a).In the case of the desilicated ds-ZSM-5-ATP catalyst, microporosity decreased within the first 10 min of reaction due to coke deposition, yet much gentler than the microporous ZSM-5-ATP and maintaining like that for the rest of the reaction time. Mesoporosity was well maintained during the entire run time. The pore-size distribution (Figure S3b) clearly showed that pore accessibility was much less impeded than for the microporous ZSM-5-ATP catalyst (Figure S3a), confirming the reported benefits of inducing mesoporosity, in terms of preserving at a great extent the textural properties of the catalyst upon reaction.[11,65] The enlargement of the pores removes barriers for coke entrance into the inner zeolites matrix pores. Rather than pore blockage, which would render active sites inaccessible to reactants, the catalyst deactivates due to active site coverage.

For ZrO_2/ds-ZSM-5-ATP (c), the effects of reaction time were more severe than for the non-promoted counterpart: microporosity, but in special mesoporosity reduced to nearly the half of the initial value. This may indicate that coke stays more externally, what contributes for its bulkier development. Compared to the microcrystalline catalysts, the textural properties of the ZrO_2/n-ZSM-5-ATP catalyst were much better maintained during pyrolysis. The Ar isotherms of the spent and fresh samples looked very similar, except for the slightly lower micro- and mesoporosity of the spent samples. The good stability shown by the nanosized catalyst with increasing time-on-stream might be connected to the coke also being partially located on the external surface, between crystal voids, as indicated by the decrease in S_{BET} (Figure S2d), which would hamper the reaction less.

The progress of the reaction also led to changes in acidity. For ZSM-5-ATP, acidity was considerably reduced after 10 min of reaction. While the Lewis acid sites were also affected, the strong Brønsted acid sites, thought to be mainly responsible for the activity in this reaction,[9] were reduced the most. This indicates that both pore occlusion, previously determined by Ar physisorption, and (strong) Brønsted active site coverage by coke species in the micropores were the main reasons of deactivation for the microporous catalyst.[65–66] No further major changes were recorded for the spent catalysts, except for a small gradual reduction in the Lewis acid sites, confirming the previous observations from TPO that intra-porous coke was mostly formed in the micropores during reaction initiation. Once these got blocked, a slower external coke deposition occurred on the zeolite surface, reducing the available reactive surface and blocking Lewis sites. For ds-ZSM-5-ATP (Figure 2b) and ZrO_2/ds-ZSM-5-ATP catalysts (c) a steep decrease in acidity was seen also, with the strong sites being more affected (Figure 2). However, the acidity drop appeared to be more gradual with time-on-stream and affected both the Brønsted and Lewis acid sites, this in contrast to the microporous catalyst. It might thus be inferred that in the desilicated catalysts, with and without ZrO_2, the main mechanism of deactivation was acid site coverage by coke, discarding pore occlusion. This is in line with the measured textural properties and the TPO results on these samples which showed that mesoporosity rendered the active sites accessible as the reaction progresses. It should be noted that in the presence of ZrO_2, the acidity changes were more severe, in line with the higher loss of micropore and mesopore volume during reaction for the ZrO_2/ds-ZSM-5-ATP catalyst. Much less affected was the acidity of the ZrO_2/n-ZSM-5-ATP catalyst upon reaction, mainly caused by site blocking due to coke deposition. The decay of the Brønsted and Lewis acid sites was more gradual and, very importantly, the strength of the Brønsted acid sites was maintained upon reaction. The perseverance of acidity seen for the nanocrystalline catalyst could be related to three key factors: 1) the milder acid strength of its active sites, related to the higher Si/Al ratio, what limits coke proliferation; 2) its less extended mesoporosity, compared to the desilicated samples, which may prevent bulk coke formation with the known effects on pores/active sites coverage; 3) its high surface area which, even after long reaction times was still available.

Coke deposition also led to changes in structural properties, as demonstrated by XRD (Figure 3). For the microcrystalline catalysts (a, b, c), the shape of some diffraction peaks suffered significant changes upon reaction. Such changes included the transformation of the initially split peak at 2θ ca. 26.9° into a single peak, and its relative increase in intensity compared to the peak at ca. 27.6° (see insets). This intensity increase was attributed to the incorporation of organics within the zeolite framework[40–41] and proportionally increased with longer reaction times due to coke accumulation. The diffraction peak at 2θ 53.1° is another example of an initially split peak converting into a single one after reaction. All these changes in the XRD patterns, together with small peak shifts, point out to a likely transition from orthorhombic to tetragonal phase (PDF 00-044-0002) during reaction.[33,37] In strong contrast, such phase change could not be detected for the spent ZrO_2/n-ZSM-5-ATP catalyst (d), in line with lower coke deposition in the pores. Another common consequence of the reaction conditions was a slight distortion of the crystallinity caused by the coke deposits and illustrated by the lower intensity of the low angle peaks at 2θ 9.2° and 10.3°,[41–42] accentuated with the longer reaction times. The XRD patterns of all spent samples also showed important enhancement of the peak at 31.0° (2θ), which can either be result of re-dispersion of the quartz phase of attapulgite under the high reaction temperatures, or of the emergence of the graphite phase coming from the hard coke formed during reaction, also typically located at 2θ 31.0-31.1° (PDF 00-026-1077, Co $K_{\alpha1,2}$).[67]

It is expected that the crystallinity loss caused by coke show-up is mostly reversible. Indeed, upon combustion of the coke deposits in a regeneration cycle one would expect that

the XRD pattern returns to its original shape, (indicative of recovered crystallinity), as seen for the nano ZrO_2/n-ZSM-5-ATP catalyst in a former study.[44] In base on that, an oxidative atmosphere (flowing air, to avoid catalyst structural damage upon the CO_2 and H_2O release) and mild (~500 °C) combustion temperature and heating rate (5 °C/min) are recommended. As for the duration, 3 h might suffice to get rid of the coke, recovering a great part of the initial catalyst properties (acidity, crystallinity, texture, structure and morphology). This method might be valid for mesoporous catalytic materials (both micro- and nanosized). Yet, it is likely that in the case of the microporous ZSM-5-ATP catalyst, a shorter regeneration cycle is required, given the lower and softer nature of the coke formed.

5. Conclusions

A series of tailored zeolite ZSM-5-based technical catalysts were tested for ex-situ Catalytic Fast Pyrolysis (CFP) of oak biomass for bio-oil production, comparing and connecting the influence of their respective physical properties with the obtained performance, tips that serve for designing optimal catalyst systems. For the set of catalysts studied, the microporous ZSM-5-ATP with attapulgite (ATP) as binder was the one with the lowest activity towards the cracking/deoxygenation reaction. Coke formation, found to be the main deactivating source, led to blocked micropores and active site coverage. Characterization by confocal fluorescence microscopy, UV-Vis diffuse reflectance spectroscopy and FT-IR micro-spectroscopy revealed that coke, which tends to form close to strong Brønsted acid sites, indeed accumulates in zeolite-rich domains and is much less present in binder-rich aggregates. The desilicated version, i.e. the ds-ZSM-5-ATP catalyst, was more active towards deoxygenation over prolonged reaction times, which is related to the introduced mesoporosity, which notably prevents pore occlusion. However, site coverage by coke was also observed. As expected, the coke deposits formed in mesoporous catalysts were bulkier than in its microporous counterparts.

The incorporation of ZrO_2 into desilicated ds-ZSM-5-ATP decreased the catalyst cracking activity, thus improving the bio-oil yield as a result of an increase in amount of Lewis acid sites. Consequently, the coke formed onto ZrO_2/ds-ZSM-5-ATP was softer in nature, i.e. less poly-aromatic, what may facilitate its removal in a regeneration step. Yet, as in the case of the desilicated counterpart, it mainly deactivated by acid sites coverage. The textural properties of the ZrO_2-containing catalyst changed more extensively during reaction than for ds-ZSM-5-ATP, suggesting that the ternary sample is not so well integrated, as was also confirmed by CFM. For both desilicated samples, with and without ZrO_2, the crystallinity decreased notably upon reaction.

Nanocrystalline ZrO_2/n-ZSM-5-ATP showed the highest activity in bio-oil deoxygenation, producing a high organic bio-oil yield (~20 wt% after 25 min of reaction) with the lowest oxygen content (~14 wt%). ZrO_2/n-ZSM-5-ATP, displaying larger surface area and lower acidity than the microcrystalline catalysts, better preserved its textural and acid properties over the course of the reaction. Thus, deactivation by pore occlusion or by site blockage was much more gradual for the nanocrystalline than for the microcrystalline catalysts, which is thought to be the result of the more homogeneous distribution of the binder and promoted zeolite material. In contrast to the other materials, the crystallinity of spent ZrO_2/n-ZSM-5-ATP was well preserved with increasing reaction time, thereby not undergoing any phase change. These results point at the nanocrystalline system as an excellent tailored catalyst for ex-situ CFP at the bench and, also potentially, at the pilot plant scale.

Experimental Section

Catalyst Materials

Four catalyst materials, as listed in Table 1, have been studied in this work: (a) a micron-sized standard zeolite ZSM-5 with a Si/Al ratio of ~18 (labelled as *ZSM-5-ATP*); (b) its desilicated version with induced mesoporosity and a Si/Al ratio of ~9 (labelled as *ds-ZSM-5-ATP*); (c) a ZrO_2-promoted desilicated ZSM-5 (labelled as *ZrO_2/ds-ZSM-5-ATP*; more details on this sample can be found in ref.[26]); and (d) a ZrO_2-promoted nanocrystalline ZSM-5 (Clariant) with a Si/Al ratio of ~42 (labelled as *ZrO_2/n-ZSM-5-ATP*).[29] All catalyst materials were extruded with attapulgite as binder material. The catalyst materials, initially shaped as catalyst bodies, were then grounded into grain sizes of 100–500 μm to avoid preferential diffusion pathways within the catalytic bed in a plug-flow reactor.

Characterization Methods and Catalytic Fast Pyrolysis Tests

Detailed information about the characterization techniques used, as well as on the procedure and set up employed for the biomass catalytic pyrolysis tests, is provided in the Supplementary Information.

Acknowledgements

The work was conducted with support from the EU under the frame of the FP7 funded "CAScade deoxygenation process using tailored nanoCATalysts for the production of BiofuELs from lignocellullosic biomassCASCATBEL" project (Grant agreement No. 604307). Dr. A. Horvat, Dr. T. Fakin and M. Zmazek (all from Silkem d.o.o) are thanked for providing the catalyst materials.

Conflict of Interest

The authors declare no conflict of interest.

Keywords: Biomass Catalytic Fast Pyrolysis · Coke · Micro-spectroscopy · Mesoporosity · Crystal Size

[1] C. Liu, H. Wang, A. M. Karim, J. Sun, Y. Wang, *Chem. Soc. Rev.* **2014**, *43*, 7594–7623.
[2] J. Cai, W. Wu, R. Liu, G. W. Huber, *Green Chem.* **2013**, *15*, 1331–1340.
[3] A. V. Bridgwater, *Biomass Bioenergy* **2012**, *38*, 68–94.

[4] E. Heracleous, A. A. Lappas, D. P. Serrano, *Biomass Convers. Biorefin.* **2017**, *7*, 275–276.
[5] U. S. M. Bertero, G. de la Puente, *Fuel* **2012**, *95*, 263–271.
[6] H. Zhang, S. Shao, R. Xiao, D. Shen, J. Zeng, *Energ. Fuel* **2014**, *28*, 52–57.
[7] M. M. Yung, A. K. Starace, C. Mukarakate, A. M. Crow, M. A. Leshnov, K. A. Magrini, *Energ. Fuel* **2016**, *30*, 5259–5268.
[8] M. M. Yung, A. R. Stanton, K. Lisa, R. J. French, K. A. Orton, K. A. Magrini, *Energ. Fuel* **2016**, *30*, 9471–9479.
[9] S. Vitolo, B. Bresci, M. Seggiani, M. G. Gallo, *Fuel* **2001**, *80*, 17–26.
[10] D. Verboekend, J. Pérez-Ramírez, *Catal. Sci. Technol.* **2011**, *1*, 879–890.
[11] D. P. Serrano, R. A. García, G. Vicente, M. Linares, D. Procházková, J. Čejka, *J. Catal.* **2011**, *279*, 366–380.
[12] J. Gou, Z. Wang, C. Li, X. Qi, P. J. Dauenhauer, T. J. Mountziaris, W. Fan, *Green Chem.* **2017**, *19*, 3549–3557.
[13] J. Hertzog, V. Carre, L. Jia, C. MacKay, L. Colin, L. Pinard, A. Dufour, O. Masek, F. Aubriet, *ACS Sustainable Chem. Eng.***2018**, *6*, 4717–4728.
[14] G. T. Whiting, F. Meirer, M. M. Mertens, A–J. Bons, B. M. Weiss, P. A. Stevens, E. de Smit, B. M. Weckhuysen, *ChemCatChem* **2015**, *7*, 1312–1321.
[15] G. T. Whiting, A. D. Chowdhury, R. Oord, P. Paalanen, B. M. Weckhuysen, *Faraday Discuss.* **2016**, *188*, 369–386.
[16] R. V. Jasra, B. Tyagi, Y. M. Badheka, V. N. Choudary, T. S. G. Bhat, *Ind. Eng. Chem. Res.* **2003**, *42*, 3263–3272.
[17] E. T. C. Vogt, G. T. Whiting, A. D. Chowdhury, B. M. Weckhuysen, *Adv. Catal.* **2015**, *58*, 143–314.
[18] S. Mitchell, N.-L. Michels, K. Kunze, J. Pérez-Ramírez, *Nat. Chem.* **2012**, *4*, 825–831.
[19] E. Kantarelis, W. Yang, W. Blasiak, *Fuel* **2014**, *122*, 119–125.
[20] G. T. Whiting, S.-H. Chung, D. Stosic, A. D. Chowdhury, L. I. van der Wal, D. Fu, J. Zecevic, A. Travert, K. Houben, M. Baldus, B. M. Weckhuysen, *ACS Catal.* **2019**, *9*, 4792–4803.
[21] P. Pérez-Uriarte, M. Gamero, A. Ateka, M. Díaz, A. T. Aguayo, J. Bilbao, *Ind. Eng. Chem. Res.* **2016**, *55*, 1513–1521.
[22] N. L. Michels, S. Mitchell, J. Pérez-Ramírez, *ACS Catal.* **2014**, *4*, 2409–2417.
[23] Y. Wang, Y. Chang, M. Liu, A. Zhang, X. Guo, *Molecules* **2019**, *24*, 3462–3476.
[24] Nishu, R. Liu, Md. M. M. Rahman, M. Sarker, M. Chai, C. Li, J. Cai, *Fuel Process. Technol.* **2020**, *199*, 106301–106316.
[25] T. C. Hoff, D. W. Gardner, R. Thilakaratne, J. Proano-Avilés, R. C. Brown, J. P. Tessonnier, *Appl. Catal. A* **2017**, *529*, 68–78.
[26] H. Hernando, A. M. Hernández-Giménez, C. Ochoa-Hernández, P. C. A. Bruijnincx, K. Houben, M. Baldus, P. Pizarro, J. M. Coronado, J. Fermoso, J. Čejkac, B. M. Weckhuysen, D. P. Serrano, *Green Chem.* **2018**, *20*, 3499–3511.
[27] S. Wan, C. Waters, A. Stevens, A. Gumidyala, R. Jentoft, L. Lobban, D. Resasco, R. Mallinson, S. Crossley, *ChemSusChem* **2015**, *8*, 552–559.
[28] T. Armaroli, L. J. Simon, M. Digne, T. Montanari, M. Bevilacqua, V. Valtchev, J. Patarin, G. Busca, *Appl. Catal. A* **2006**, *306*, 78–84.
[29] H. Hernando, A. M. Hernández-Giménez, S. Gutiérrez-Rubio, T. Fakin, A. Horvat, R. M. Danisi, P. Pizarro, J. Fermoso, E. Heracleous, P. C. A. Bruijnincx, A. A. Lappas, B. M. Weckhuysen, D. Serrano, *ChemSusChem* **2019**, *12*, 2428–2438.
[30] P. A. Horne, P. T. Williams, *J. Anal. Appl. Pyrolysis* **1995**, *34*, 65–85.
[31] K. S. W. Sing, D. H. Everett, R. A. W. Haul, L. Moscou, R. A. Pierotti, J. Rouquerol, *Int. Union Pure Appl. Chem.* **1985**, *57*, 603–619.
[32] K. S. W. Sing, R. T. Williams, *Adsorpt. Sci. Technol.* **2004**, *22*, 773–782.
[33] B. Louis, A. Vicente, C. Fernández, V. Valtchev, *J. Phys. Chem. C* **2011**, *115*, 18603–18610.
[34] A. M. Hernández-Giménez, Ch. 5 in *Catalyst Deactivation and Regeneration during Bio-Oil Upgrading Processes*, Utrecht University, **2018**.
[35] H. Hernando, C. Ochoa-Hernández, M. Shamzy, I. Moreno, J. Fermoso, P. Pizarro, J. M. Coronado, J. Čejka, D. P. Serrano, *Catal. Sci. Technol.* **2019**, *9*, 789–802.
[36] N. Katada, M. Niwa, *Catal. Surv. Asia* **2004**, *8*, 161–170.
[37] F. Lónyi, J. Valyon, *Microporous Mesoporous Mater.* **2001**, *47*, 293–301.
[38] L. Rodríguez-González, F. Hermes, M. Bertmer, E. Rodríguez-Castellón, A. Jiménez-López, U. Simon, *Appl. Catal. A* **2007**, *328*, 174–182.
[39] A. S. Al-Dughaither, H. De Lasa, *Ind. Eng. Chem. Res.* **2014**, *53*, 15303–15316.
[40] A. G. Alvarez, H. Viturro, R. D. Bonetto, *Mater. Chem. Phys.* **1992**, *32*, 135–140.
[41] D. Rojo-Gama, M. Signorile, F. Bonino, S. Bordiga, U. Olsbye, K. P. Lilleurd, P. Beato, S. Svelle, *J. Catal.* **2017**, *351*, 33–48.
[42] E. L. Wu, S. L. Lawton, D. H. Olson, A. C. Rohrman, G. T. Kokotailo, *J. Phys. Chem.* **1979**, *8*, 2777–2781.
[43] J. Zhang, X. Liu, *Phys. Chem. Chem. Phys.* **2014**, *16*, 8655–8660.
[44] E. Heracleous, E. Pachatouridou, A. M. Hernández-Giménez, H. Hernando, T. Fakin, A. L. Paioni, M. Baldus, D. P. Serrano, P. C. A. Bruijnincx, B. M. Weckhuysen, A.A Lappas, *J. Catal.* **2019**, *380*, 108–122.
[45] A. Pulido, B. Oliver-Tomas, M. Renz, M. Boronat, A. Corma, *ChemSusChem* **2013**, *6*, 141–151.
[46] S. Cheng, L. Wei, X. Zhao, J. Julson, *Catalysts* **2016**, *6*, 195–219.
[47] M. Ibáñez, B. Valle, J. Bilbao, A. G. Gayubo, P. Castaño, *Catal. Today* **2012**, *195*, 106–113.
[48] C. Mukarakate, X. Zhang, A. R. Stanton, D. J. Robichaud, P. N. Ciesielski, K. Malhora, B. S. Donohoe, E. Gjersing, R. J. Evans, D. S. Heroux, R. Richards, K. lisa, M. R. Nimlos, *Green Chem.* **2014**, *161*, 444–1461.
[49] B. Valle, P. Castaño, M. Olazar, J. Bilbao, A. G. Gayubo, *J. Catal.* **2012**, *285*, 304–314.
[50] J. Kim, M. Choi, R. Ryoo, *J. Catal.* **2010**, *269*, 219–228.
[51] A. N. Parvulescu, D. Mores, E. Stavitski, C. M. Teodorescu, P. C. A. Bruijnincx, R. J. M. K. Gebbink, B. M. Weckhuysen, *J. Am. Chem. Soc.* **2010**, *132*, 10429–10439.
[52] H. Yang, A. Tang, J. Ouyang, M. Li, S. Mann, *J. Phys. Chem. B* **2010**, *114*, 2390–2398.
[53] D. Mores, J. Kornatowski, U. Olsbye, B. M. Weckhuysen, *Chem. Eur. J.* **2011**, *17*, 2874–2884.
[54] E. C. Nordvang, E. Borodina, J. Ruiz-Martínez, R. Fehrmann, B. M. Weckhuysen, *Chem. Eur. J.* **2015**, *21*, 17324–17335.
[55] Q. Qian, J. Ruiz-Martinez, M. Mokhtar, A. M. Asiri, S. A. Al-Thabaiti, S. N. Basahel, H. E. van der Bij, J. Kornatowski, B. M. Weckhuysen, *Chem. Eur. J.* **2013**, *19*, 11204–11215.
[56] G. T. Whiting, N. Nikolopoulos, I. Nikolopoulos, A. D. Chowdhury, B. M. Weckhuysen, *Nat. Chem.* **2019**, *11*, 23–31.
[57] M. Guisnet, P. Magnoux, *App. Catal.* **1989**, *54*, 1–27.
[58] M. Guisnet, P. Magnoux, *App. Catal. A: Gen.* **2001**, *212*, 83–93.
[59] P. Magnoux, P. Cartraud, S. Mignard, M. Guisnet, *J. Catal.* **1987**, *106*, 235–241.
[60] S. Bordiga, C. Lamberti, F. Bonino, A. Travert, F. Thibault-Starzyk, *Chem. Soc. Rev.* **2015**, *44*, 7262–7341.
[61] A. Corma, P. J. Miguel, A. V. Orchillés, *J. Catal.* **1994**, *145*, 171–180.
[62] M. Guisnet, P. Magnoux, *Catal. Today* **1997**, *36*, 477–483.
[63] M. Boronat, P. Viruela, A. Corma, *J. Phy. Chem. B* **1999**, *103*, 7809–7821.
[64] A. D. Chowdhury, I. Yarulina, E. Abou-Hamad, A. Gurinov, J. Gascon, *Chem. Sci.* **2019**, *10*, 8946–8954.
[65] F. Schmidt, C. Hoffman, G. Filippo, S. Bordiga, P. Simon, W. Carrill-Cabrera, S. Kaskel, *J. Catal.* **2013**, *307*, 238–245.
[66] H. A. Benesi, B. H. C. Winquist, D. D. Eley, H. Pines, P. B. Weisz, *Adv. Catal.* **1978**, *27*, 98.
[67] Y. Fan, Y. Cai, X. Li, H. Yin, J. Xia, *J. Ind. Eng. Chem.* **2017**, *46*, 139–149.

Manuscript received: November 1, 2020
Revised manuscript received: November 29, 2020
Accepted manuscript online: December 1, 2020
Version of record online: December 28, 2020